WARWICK
THE UNIVERSITY OF WARWICK

Manuscript version: Author's Accepted Manuscript
The version presented in WRAP is the author's accepted manuscript and may differ from the published version or Version of Record.

Persistent WRAP URL:
http://wrap.warwick.ac.uk/109835

How to cite:
Please refer to published version for the most recent bibliographic citation information. If a published version is known of, the repository item page linked to above, will contain details on accessing it.

Copyright and reuse:
The Warwick Research Archive Portal (WRAP) makes this work by researchers of the University of Warwick available open access under the following conditions.

Copyright © and all moral rights to the version of the paper presented here belong to the individual author(s) and/or other copyright owners. To the extent reasonable and practicable the material made available in WRAP has been checked for eligibility before being made available.

Copies of full items can be used for personal research or study, educational, or not-for-profit purposes without prior permission or charge. Provided that the authors, title and full bibliographic details are credited, a hyperlink and/or URL is given for the original metadata page and the content is not changed in any way.

Publisher's statement:
Please refer to the repository item page, publisher's statement section, for further information.

For more information, please contact the WRAP Team at: wrap@warwick.ac.uk.

warwick.ac.uk/lib-publications

Effect of alloying and coiling temperature on the microstructure and bending performance of ultra-high strength strip steel

Abhisek Mandal[1*], Anish Karmakar[2], Debalay Chakrabarti[1], and Claire Davis[3]

[1]*Department of Metallurgical and Materials Engineering, IIT Kharagpur, Kharagpur 721302, India*
[2]*Department of Metallurgical and Materials Engineering, NIT Warangal, Telangana 506004, India*
[3]*Warwick Manufacturing Group, University of Warwick, Zip-CV4 7AL, England, UK*

*Corresponding Author, Mailing ID: abhisekm9@gmail.com, Phone: +91 9547374713

ABSTRACT

Two different high strength B-containing microalloyed steel strips produced in industrial processing conditions, one treated with Ti and the other treated with Al, processed by controlled rolling, accelerated cooling and coiling in two different temperatures ranges [723 K to 733 K (450 °C to 460 °C)] and [633 K to 653 K (360 °C to 380 °C)] were subjected to bend testing. The Ti treated steel coiled at the higher temperature 733 K (460 °C) showed the best bending performance. The relatively softer (tensile strength of < 900 MPa) and homogeneous microstructure containing mostly granular bainite and upper bainite to ~300-400 μm depth below the surface, generated at the higher coiling temperature, is preferred for bendability. The lower temperature coiling resulted in the formation of a hard surface layer dominated by martensite which is undesired as the steel becomes prone to shear cracking and interphase separation due to strain-localization. The combined effect of beneficial texture components such as γ-fiber, {332} <113> and even {112} <131> in the sub-surface region as well as uniformity of through thickness texture of the rolled sheet improve the bendability. In the presence of crack initiators, like coarse and brittle TiN particles found in the Ti treated steel, a harder microstructure and the presence of Cube and Goss texture in the sub-surface layer, seen for the lower coiling temperature can cause local transgranular cleavage cracking. Finally the post-uniform elongation obtained from tensile testing and bendability follow a good correlation.

Keywords: High strength steel strip; Coiling temperature; Bainite; Martensite; Bend test; Microstructural homogeneity; Crystallographic texture

1. INTRODUCTION

There has been an increasing interest to develop ultra-high strength steels (UHSS), i.e. steels with yield strength greater than 700 MPa, for various applications, such as transportation, construction, engineering, shipbuilding, energy and defence [1]. Such a development is based on the requirement of structures with lighter weight and reduced material thickness without sacrificing safety and structural integrity. Thus significant cost and energy savings can be achieved as a result of a reduced requirement of material and welding consumables, better energy efficiency and even improved fracture toughness due to the reduced section thickness [1,2]. However, a major challenge concerning the application of UHSS is its poor formability [3]. UHSS in the form of thick strip is primarily used in structural components which are formed by bending. Hence, satisfactory bendability is an essential requirement of UHSS [2,4].

Bending is a conventional sheet metal forming process [5], where the deformation behavior of the material differs from that of simple tensile testing [6]. During bending the outer layers of the metal piece are subjected to higher tensile strains as compared to the inner layers. Hence the yield strength is exceeded first at the outer layers [7]. Uniform deformation continues till the point at which the increase in stress can accommodate plastic strengthening. Subsequent bending results in non-uniform plastic deformation leading to the onset of diffused necking [8–10]. Eventually, strain increasingly localizes into a narrow band, termed as a shear band [11,12]. According to several studies, strain localization and the formation of shear bands is the precursor for damage in bending. Therefore, a considerable scientific effort has been made to identify the factors contributing to the evolution of shear bands during bending operation [3,13–15]. Those factors are commonly related to the specific mechanical properties of the material such as strength and work-hardening capability. Such properties depend on the microstructural constituents and their homogeneity, crystallographic texture, inclusions and defects and surface roughness [2,14,16–19]. It has been established that the local-scale deformation behavior instead of the total elongation governs the bendability of UHSS[20,21]. It has been suggested that inhomogeneity in the microstructure act as local hot-spots for stress and strain and contribute to the failure during bending [2,22]. A homogeneity index, based on the deviation in hardness measurements, was proposed to evaluate the homogeneity of the microstructure [2,23]. In addition to microstructural uniformity, the beneficial effect of a soft surface layer on bendability has been widely recognized [14,19,24,25]. A soft surface layer provides increased deformation capability at the region, which is subjected to the maximum strains [25].

Research emphasis has mostly been on improving the strength and toughness of UHSS grades. Therefore, there is a lack of information on the effect of processing parameters on bendability of UHSS. Thus the primary aim of this study is to understand the influence of processing and composition on the microstructure, and hence on bendability, of boron containing microalloyed UHSS. To establish the microstructure-bendability correlation, there is a need to identify the exact mechanism governing cracking during bending. In particular, the effects of surface hardness and microstructural homogeneity on the bendability need to be understood and are discussed in this paper.

2. EXPERIMENTAL DETAILS

Four samples with dimensions of 600 mm length, 300 mm width and 6-8 mm thickness were received from Tata Steel in Europe. The samples were taken from boron containing ultrahigh strength microalloyed steel strips. These steel strips were produced in industrial trials at Tata Steel and were part of a larger development program of UHSS intended to determine which combination of chemical composition and processing parameters was optimal. To retain boron in solution by avoiding BN formation, it is necessary to treat the steel with a stronger nitride former, such as Ti or Al. The investigated steels were either Al-treated or Ti-treated and their chemical compositions are given in **Table 1**.

The strips were controlled rolled, with finish rolling temperatures of around 1223 K (950 °C), accelerated cooled and coiled at two different temperature ranges; higher [723 K to 733 K (450 °C to 460 °C)] and lower [633 K to 653 K (360 °C to 380 °C)] coiling start temperatures. The schematic diagram in **Fig. 1** shows the typical processing schedule.

The steel samples were coded by the treatment adopted (Al- or Ti-) followed by the respective coiling start temperature, i.e. Al-450, Al-360, Ti-460 and Ti-380. The Ti-380 sample was 8 mm thick and the other samples were 6 mm thick. Actual coiling start temperatures could be a little higher than the measured values as the pyrometers monitor the temperature at a distance away from the coils. The presence of some water or moisture on the strip surface at the start of coiling can also cause errors in the temperature measured.

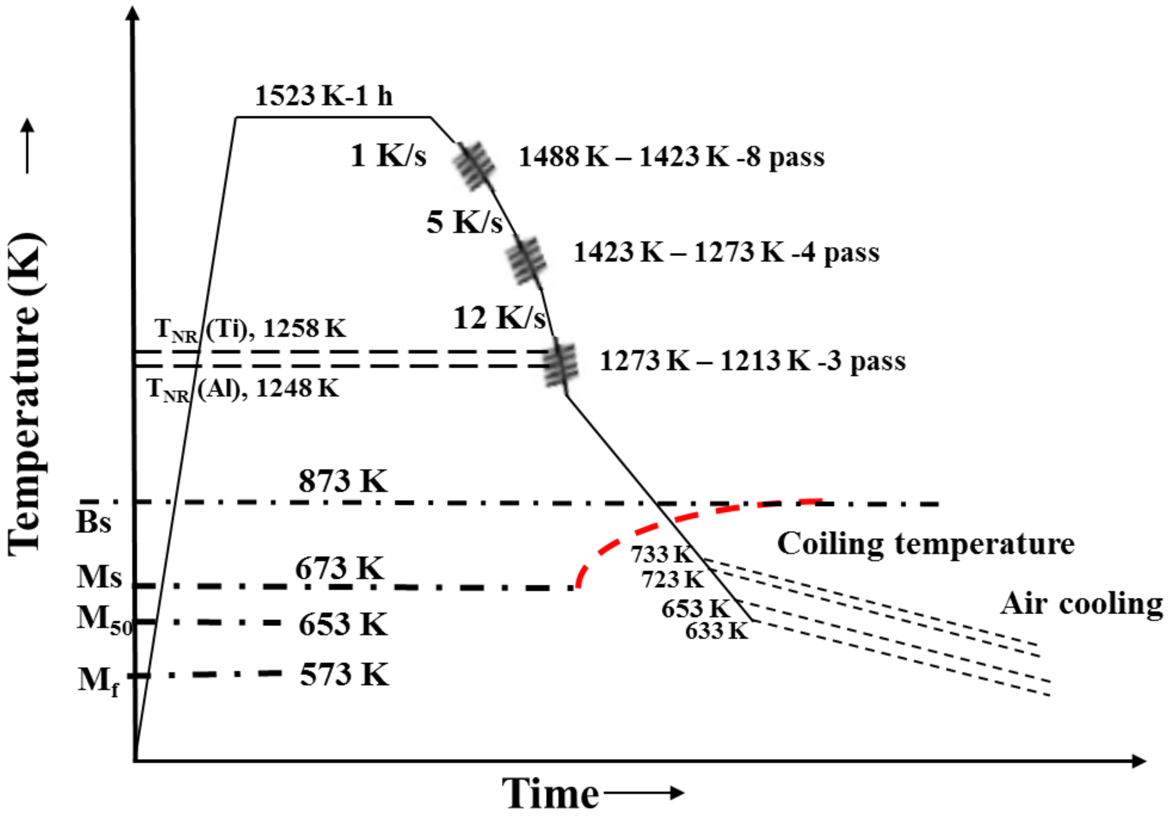

Fig. 1: Schematic diagram of the thermomechanical processing schedule applied on the investigated strips along with the bainitic and martensitic transformation start temperatures as predicted from JMatPro® software. Bs - bainitic start temperature, Ms - martensitic start temperature, M_{50} - 50% martensite formation temperature M_f - martensite finish temperature. T_{NR}- Recrystallization stop temperature.

Thermodynamic calculations were performed using Thermo-Calc® 4.1 software based on the nominal steel compositions to predict the formation of different phases and precipitates under equilibrium cooling conditions. Cross-sections (RD-ND plane) of the samples were prepared following standard metallographic techniques and investigated by optical microscopy (model-Leica DM600M) with the attachment of image analysis, and scanning electron microscopy (SEM model Zeiss EVO 60), with the attachment of energy dispersive spectroscopy (EDS). The microstructural study was carried out by SEM on five different locations across the sheet thickness. From each locations a 300 µm × 300 µm area was covered by SEM study. Thus the microstructural characterization was performed over an area of approximately 1.5 mm × 1.5 mm for each sample. Microstructural constituents such as GB, UB, LB and TM were identified separately in those high magnification (3000x) SEM images and their fractions were determined by image analysis. Panalytical High Resolution

X-ray Goniometer (Model PW 3040/60) was used for the macrotextural study (on RD-TD plane). Thin foils (~ 30 nm) were prepared by electropolishing using a solution of 80 percent methanol and 20 percent perchloric acid. These foils were studied by high-resolution transmission electron microscope, TEM (JEOL-2000 FX, Japan). Vickers macrohardness readings were taken through the thickness at different locations i.e., sub-surface (350 µm from free surface), quarter thickness and mid thickness of the strip, on the RD-ND plane of the strip samples at 20 Kgf load with 15 s dwell time using LV-700 model LECO® hardness tester. Heterogeneity of the microstructure at those above mentioned locations of the strip was estimated by the variation in 200 hardness measurements and represented by the heterogeneity index (HI). The equation used to determine HI is given below.

$$\mathrm{HI} = \frac{\mathrm{S}}{\mathrm{H_{av}}} \times 100 \qquad (1)$$

where, $\mathrm{H_{av}}$ and S represent the average macrohardness value and the standard deviation in hardness measurement, respectively. Tensile specimens were prepared following ASTM E-8 standard and tested in a 250 ton Universal Testing Machine Instron®8801 at room temperature [~ 298 K (~ 25 °C)] and a strain rate of $6.6\text{x}10^{-5}$/s.

Bend testing was performed by following the ASTM E290 Bend Testing standard. The samples for bend testing were taken from the RD-TD plane of the rolled strip as shown in **Fig. 2a**. Schematic diagram of the bend testing setup is shown in **Fig. 2b**. Macroscopic images of the bent samples with cross sections of the bent portions are also illustrated in **Fig. 2(c-e).** All the investigated samples were bent under notch free three-point using a 250 ton Instron®8801 Universal Testing Machine. The load vs. displacement plot was recorded based on three samples for each coiling treatment; examples are given in **Fig. 2f**. The bending of a sample continued till the load dropped and visible cracks appeared on the outer 'tensile' surface. The inner-bend-angle between the two arms of a bend tested sample was measured as shown in **Fig. 2c**. The lower the inner-bend-angle, the better the bendability. Bendability was represented by the bend-ratio, i.e. the ratio of minimum bend radius to sheet thickness [26].

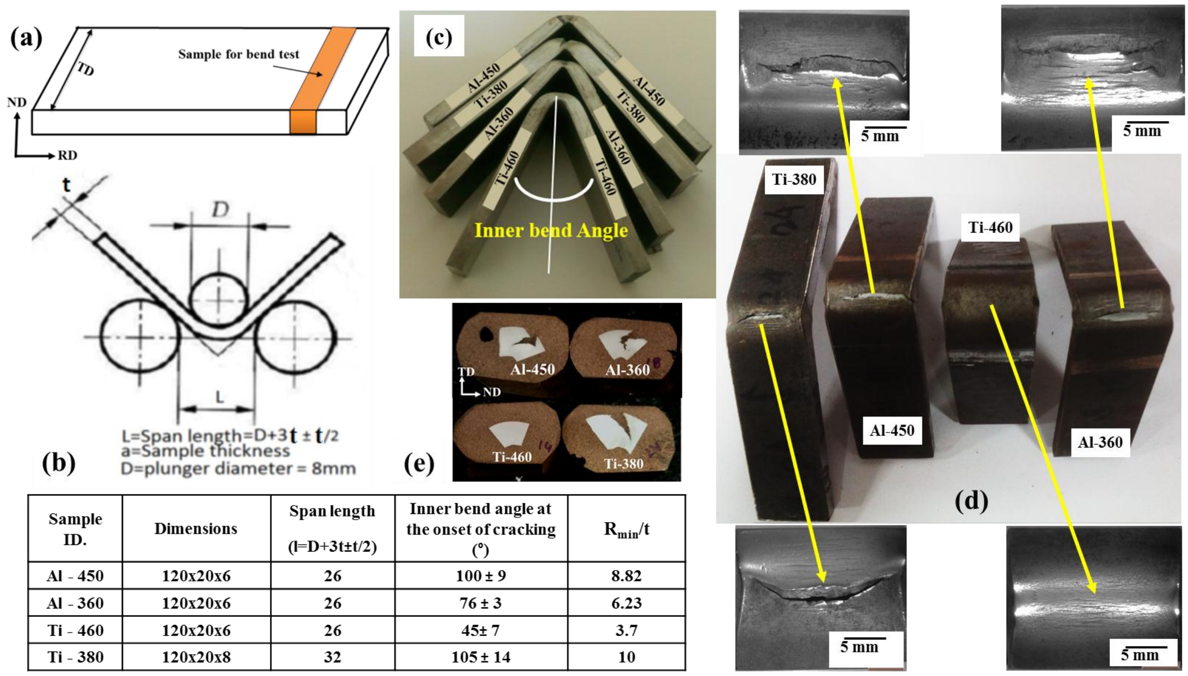

Sample ID.	Dimensions	Span length (l=D+3t±t/2)	Inner bend angle at the onset of cracking (°)	R_{min}/t
Al - 450	120x20x6	26	100 ± 9	8.82
Al - 360	120x20x6	26	76 ± 3	6.23
Ti - 460	120x20x6	26	45± 7	3.7
Ti - 380	120x20x8	32	105 ± 14	10

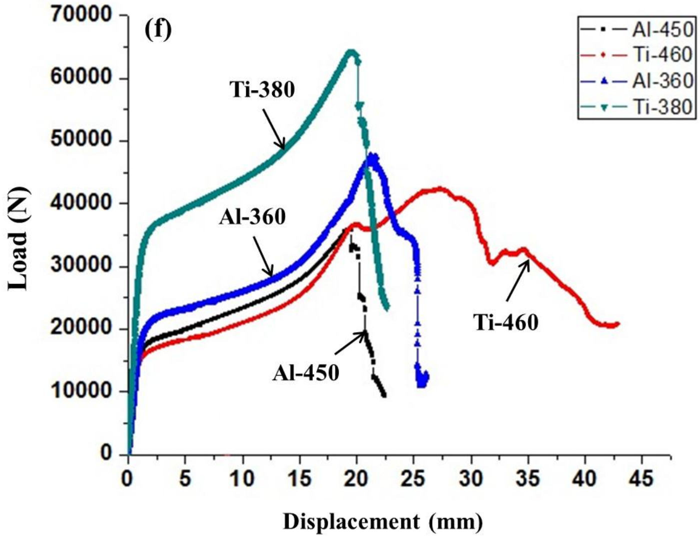

Fig. 2: (a-b) Schematic diagrams showing the orientation of the bend test specimens with respect to the strip and bend testing setup. (c) Macroscopic side-view of the bend tested specimens showing the minimum inner bend angles (until visible cracking and load-drop) with their values listed below along with the minimum bend ratio. (d) Corresponding macro-views of the cracks (at different magnifications) on the outer surface of the bend tested samples. (e) Showing the cracked regions mounted in Bakelite. (f) Load vs. displacement (at the middle of the specimen) plots obtained from bend testing.

3. RESULTS AND DISCUSSION

3.1 Thermodynamic calculation

Thermo-Calc® software estimated the ferrite transformation start temperature, A_{e3} [~ 1373 K (~ 1100 °C)], and the end temperature, A_{e1} [~ 1173 K (~ 900 °C)], under equilibrium cooling to be the same for both the steels. Thermo-Calc® also predicted the formation of different kinds of precipitates as shown in **Fig. 3**.

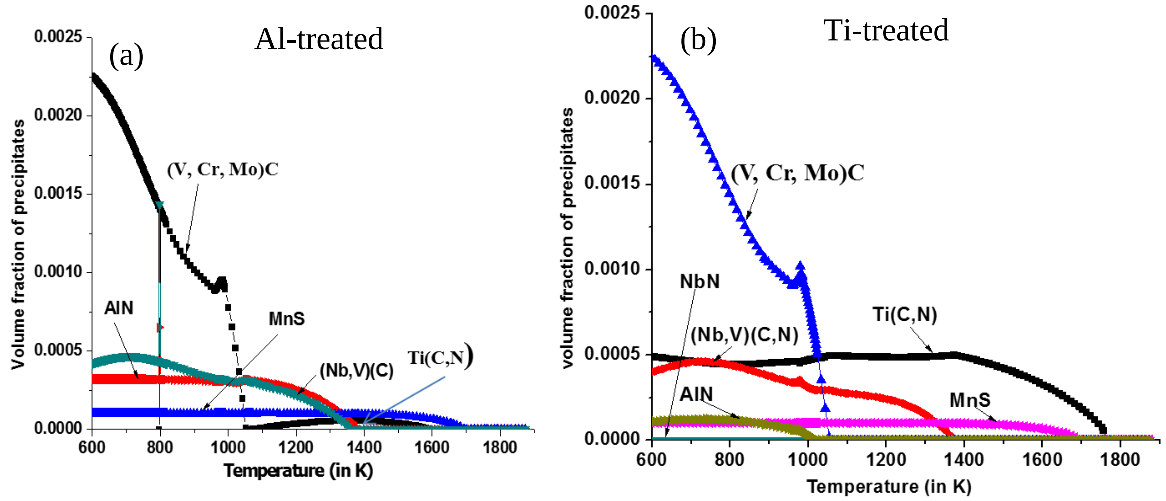

Fig. 3: Prediction of precipitate volume fraction with temperature in (a) Al-treated and (b) Ti-treated steels as predicted from Thermo-Calc®.

Fig. 3 suggest that the Ti-treated steel had a higher precipitation start temperature [by 445 K (172 °C)] and volume fraction of Ti(C,N) (more than ten times) as compared to the Al-treated steel. The estimated precipitation temperature and volume fraction of AlN are lower in the Al-treated steel as compared to those for Ti(C,N) in the Ti-treated steel. Equilibrium prediction suggested no formation of BN as evidenced in **Fig. 3**. Therefore, it is assumed that B is protected in both the investigated steels to influence hardenability. Thermo-Calc® anticipated the formation of Nb-rich (Nb,V)(C,N) and V-rich complex carbides containing Cr and Mo at around 1373 K (1100 °C) and 1053 K (780 °C), respectively, in both the steels. Fractions of those precipitates increased with the decrease in temperature. V-rich carbides in microalloyed steels primarily form during and after the transformation of austenite as the steel cools down [27], with fine VC being seen in hot rolled and coiled strip with coiling temperatures in the range examined in this work [28]. Presence of a small fraction of MnS is also expected.

3.2 Microstructural characterization

Low-magnification optical micrographs of the sub-surface regions of Al-treated (Al-450 and Al-360) and Ti-treated (Ti-460 and Ti-380) samples are illustrated in **Fig. 4.** No surface decarburized layer was present. The microstructures are comprised of different forms of bainite such as granular bainite (GB), upper bainite (UB) and lower bainite (LB) along with tempered martensite (TM) at different fractions. Higher magnification SEM images in **Fig. 5** focus on the different microstructural constituents and their distribution at the sub surface region. Typical higher magnification SEM micrograph, showing the dominance of granular bainite (MA constituents are indicated) and upper bainite in Ti-460 sample**,** is given in **Fig. 6a**. The micrograph for Al-360 sample showing a predominantly tempered martensite and lower bainite microstructure, is presented in **Fig. 6b**. Islands of martensite-austenite constituents were distributed in the bainitic ferrite matrix of GB. Upper bainite consists of inter lath carbides along the lath boundaries. On the other hand in the case of lower bainite, carbides are precipitated within the bainitic ferrite at an angle of approximately 55° to its long axis. Whereas, in tempered martensite a more random distribution of very fine carbides are observed within the martensitic laths. Detailed discussion on the formation and characteristics of each microstructural constituent is available in the literature [29]. Fractions of the microstructural constituents were quantified and are listed in **Table 2**.

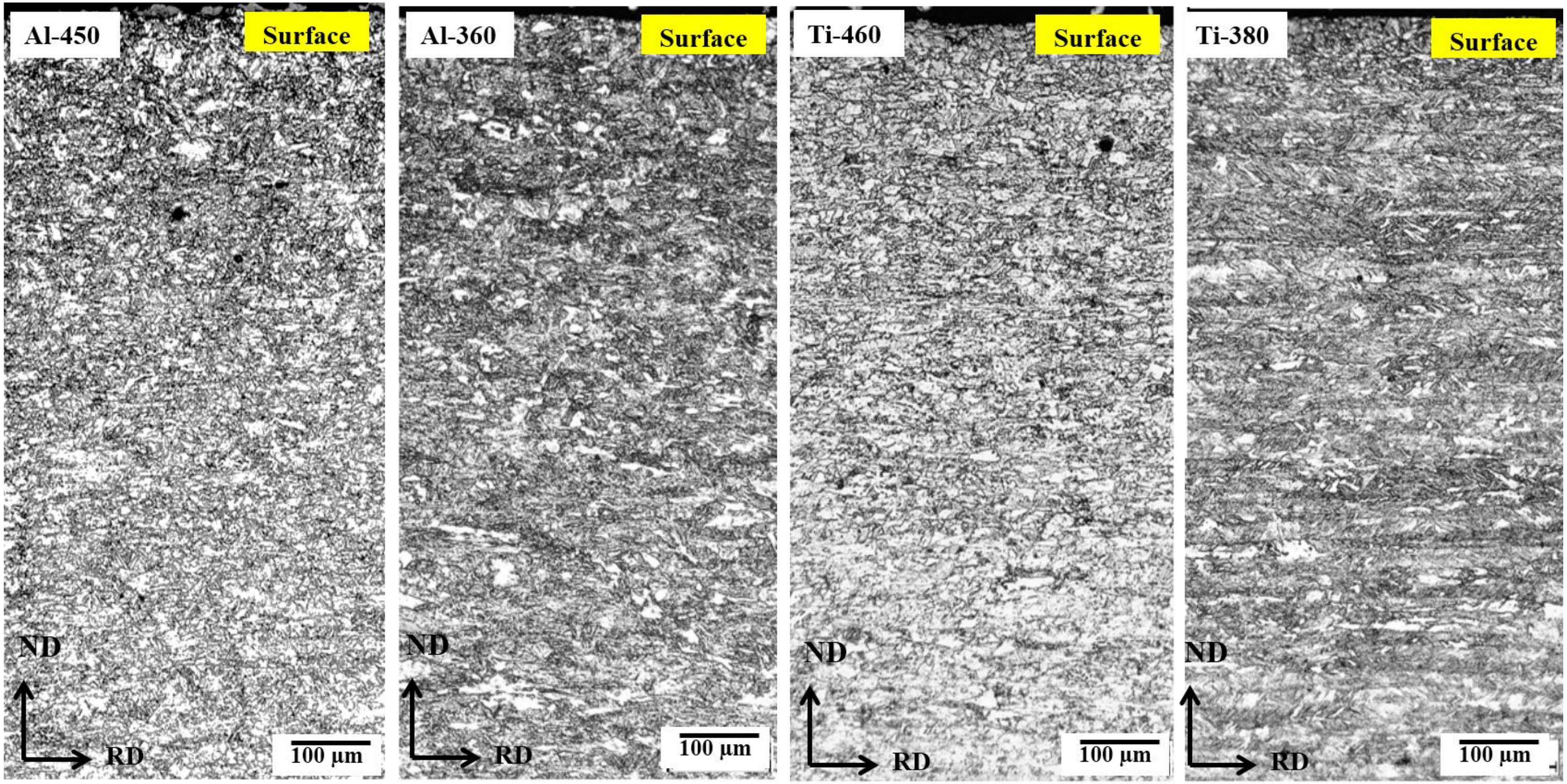

Fig. 4: Optical micrographs of the region from the top-surface up to ~ 600 µm depth along the thickness direction of RD-ND plane of the Al-treated (Al-450 and Al-360) and Ti-treated (Ti- 460 and Ti-380) strips.

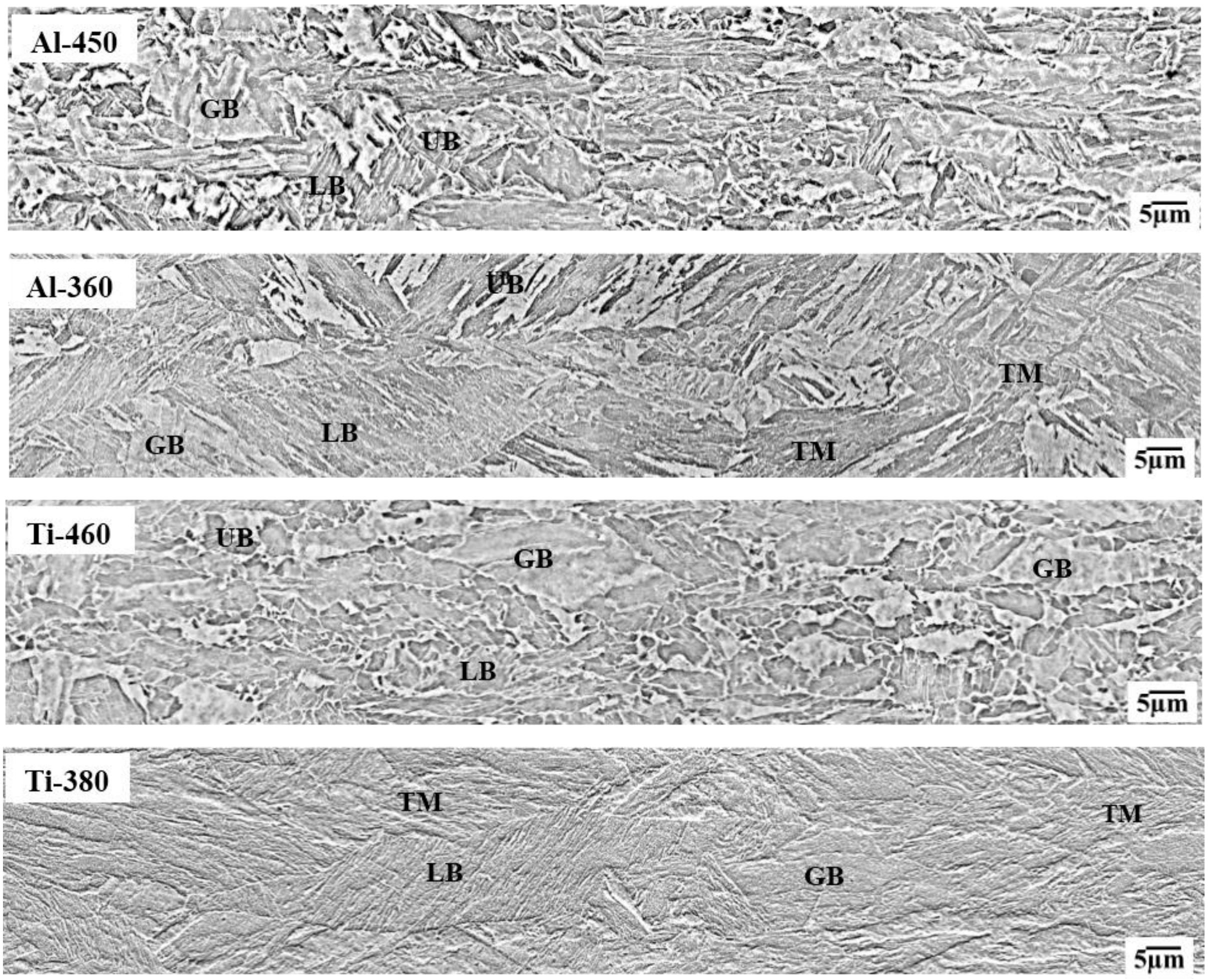

Fig. 5**:** Higher magnification scanning electron micrographs (SEM) of the investigated samples (mentioned within the respective image) at the sub surface region (~300-400μm from the top surface). Abbreviations: GB: Granular bainite, UB: Upper bainite, LB: Lower bainite, TM: Tempered martensite.

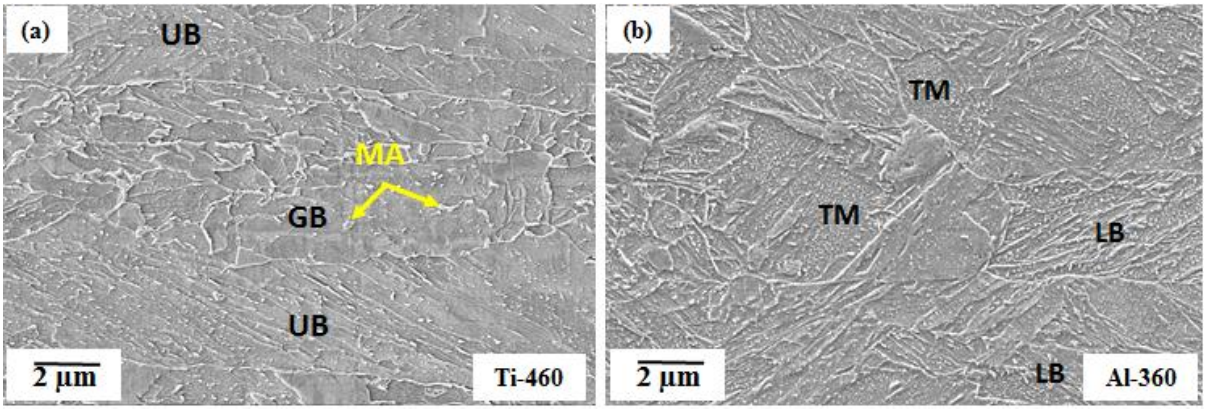

Fig. 6: Higher magnification SEM micrographs of (a) Ti-460 and (b) Al-360 samples. MA constituents are marked by yellow arrow. Abbreviations: GB: Granular bainite, UB: Upper bainite, LB: Lower bainite, TM: Tempered martensite.

Fig. 5, **Fig. 6** and **Table 2** show that the microstructures of the samples coiled at higher temperatures (Al-450 and Ti-460) and lower temperatures (Al-360 and Ti-380) were dominated by upper bainite (59-65%) and tempered martensite (48-58%), respectively. The relative fractions of UB and TM were higher in the Al-treated steel as compared to the Ti-treated steel. The fraction of GB was highest in Ti-460, followed by Al-450, whilst Al-360 had the lowest GB fraction. Al-360 and Ti-380 contained 24-30% LB besides TM.

JMatPro® software was used to predict the start temperatures of the bainitic transformation [Bs ~ 873 K (~ 600 °C)] and martensitic transformation [Ms ~ 673 K (~ 400 °C)] for the investigated steels. According to the literature the nature of bainite depends on the undercooling below B_s [29]. The higher the coiling temperature, the lower the undercooling and the larger the fractions of softer constituents like GB and UB that forms, as in Ti-460. The lower coiling start temperature, below Ms, resulted in high fraction of TM in Al-360 and Ti-380, **Table 2**.

The TEM study helped in identifying the microstructural features, **Fig. 7**. Bright field TEM images in **Fig. 7(a-c)** shows the presence of UB with carbide films situated along the lath-boundaries in Al-450 and Ti-460. In order to confirm the presence of carbide in the form of cementite selected area diffraction pattern was indexed (given as an insert in **Fig. 7b** along with the corresponding dark field image), which indicates inter lath carbide precipitation. LB with carbide precipitates inclined at certain angles within the ferritic laths was also observed, **Fig. 7d**. TM structure in Al-360 and Ti-380 comprised of martensitic laths with numerous fine precipitates as shown in **Fig. 7(e, f)**. Cuboidal shaped TiN and (Ti,Nb)(C,N) of 30-50 nm diagonal length were detected in all the samples, especially in the Ti-treated steel, **Fig. 7g**. Maximum size of those precipitates was also higher in Ti-treated steel (50 nm) than in the Al-treated steel (20 nm). The numerous spherical precipitates were iron-carbides (30-100 nm) and V-rich carbides (less than 30 nm), **Fig. 7h**.

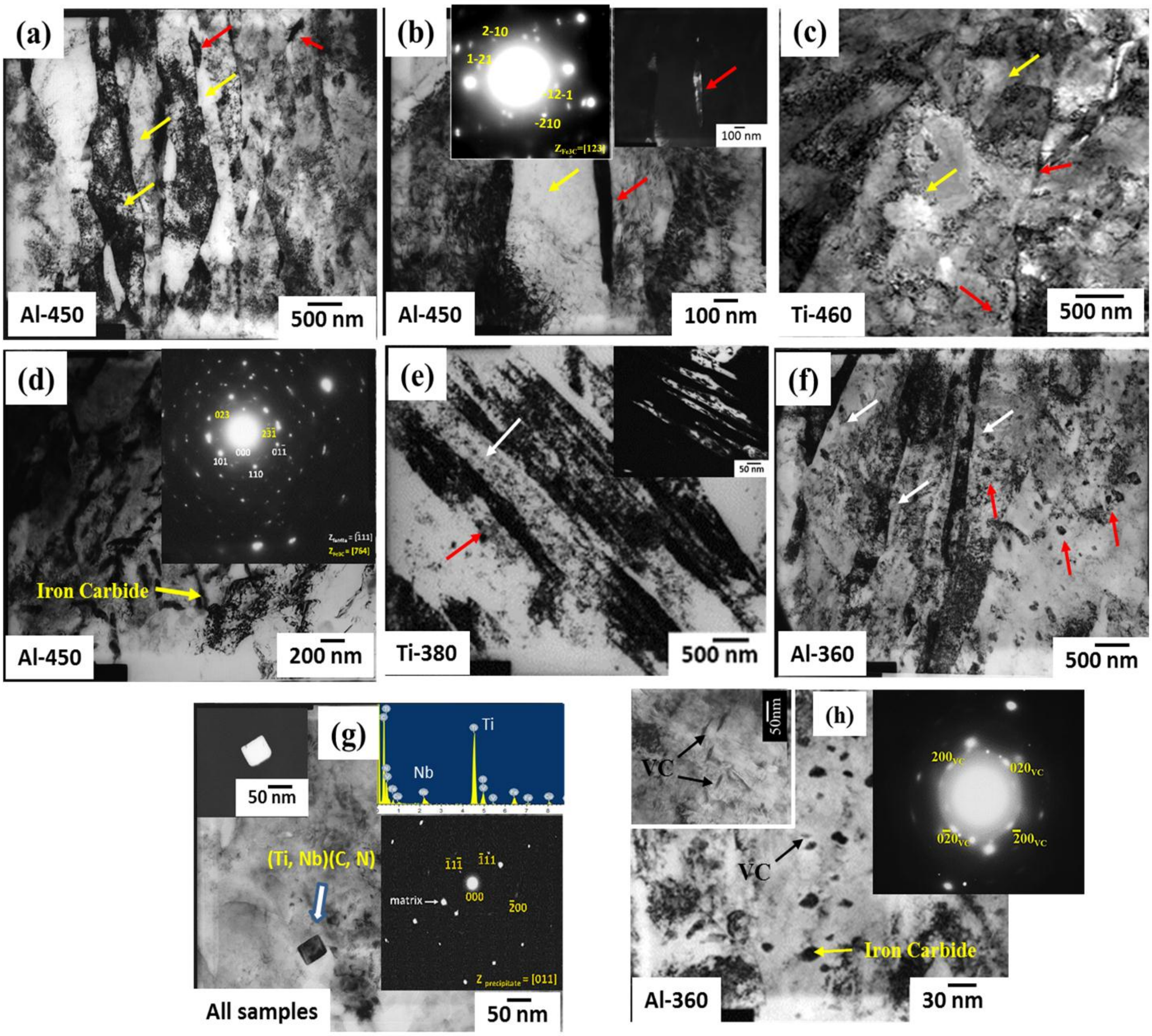

Fig. 7: (a-f) Bright field, dark field, selected area diffraction patterns (SADP) and energy dispersive spectroscopy (EDS) of the investigated samples coiled at different temperatures as indicated by the sample codes given on the respective micrographs. The bainitic laths, martensitic laths and cementite precipitates are indicated by yellow, white and red arrows, respectively. SADP and EDS spectrums are taken from (Ti,Nb)(C,N), iron-carbide and vanadium carbide precipitates as given in figures (g-h). The precipitates are also marked in the corresponding images.

The observation of fine V-rich carbides is consistent with other studies on high strength microalloyed strip steel [28]. Vanadium addition and the consequent VC formation can help in retaining the strength of bainitic hot strip steel after coiling treatment [28]. Interestingly neither AlN nor BN was detected in any of the samples. Even if those precipitates formed, their size and / or fraction were lower than the precipitate detection limit or so few as to not be present in the TEM foils examined.

3.3 Assessment of microstructural heterogeneity by hardness testing

Average Vickers macrohardness (20 Kgf) was measured through the thickness on the cross-section (RD-ND plane) of each sample as plotted in **Fig. 8a**. The decrease in coiling temperature significantly increased the hardness level. Ti-460 showed the minimum hardness followed by Al-450. Al-360 and Ti-380 had equally high hardness. Hardness of Al-360 and Ti-380 increased from sub-surface (0.2 mm from the surfaces) towards quarter-thickness and mid-thickness. In contrast hardness of Al-450 and Ti-460 decreased slightly from sub-surface towards mid-thickness, **Fig. 8a**.

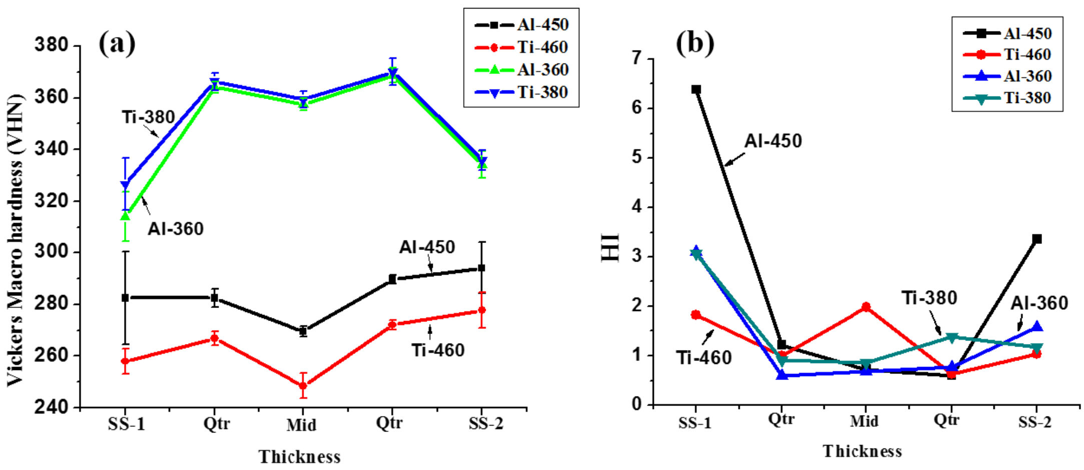

Fig. 8: (a) Average Vickers macrohardness through the thickness of the strip samples; (b) Variation in heterogeneity index (HI) through the thickness of the strip samples. Abbreviations: SS-1: Top sub surface, Qtr: Quarter thickness, Mid-Mid thickness and SS-2: Bottom sub surface.

Microstructural heterogeneity was quantified at different locations based on hardness variation as represented by the Heterogeneity Index (HI) in **Fig. 8b**. High and low HI value represents heterogeneous and homogeneous distributions of microstructural constituents in terms of hardness, respectively. Ti-460 showed superior homogeneity at sub-surface and quarter-thickness whilst heterogeneity increased towards the mid-thickness, **Fig. 8b**. Al-450, on other hand, had the most heterogeneous microstructure at the sub-surface and the heterogeneity was more severe than the rest of the samples. Samples coiled at lower temperatures (Al-360 and Ti-380) showed an intermediate level of microstructural homogeneity, **Fig. 8b**.

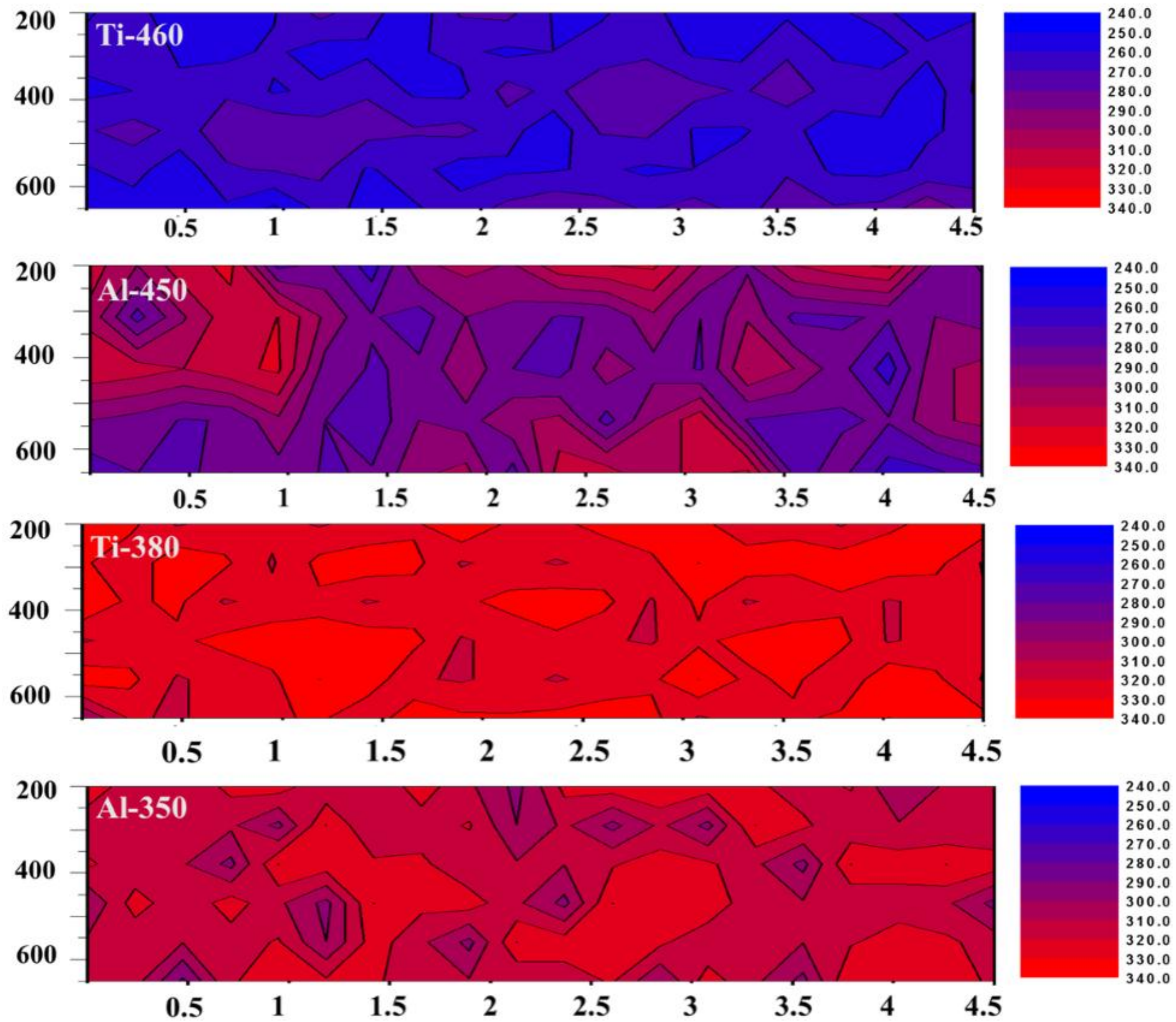

Fig. 9: Hardness contour plots at the sub-surface region of the investigated strips (RD-ND plane). X-axis is in mm. and Y-axis is in µm. Color codes represent Vickers macrohardness values as given in the legends. Note that same hardness scale is used in all the plots.

Fig 9, which clearly illustrate the microstructural heterogeneity with respect to hardness. Al-450 had sub-surface hardness ranging from 272-322 VHN, whereas in Ti-450 this variation was in the range of 253-270 VHN. Samples coiled at the lower coiling temperature

(Ti-380, Al-360) had a minimal hardness variation ranging over 310-330 VHN and high hardness due to the presence of harder microstructural constituents, **Fig 9.**

3.4 Assessment of textural heterogeneity by XRD texture analysis

Fig. 10 shows the ϕ_2 = 45° ODF sections obtained from the macrotexture study at the sub-surface (**Fig. 10(a-d)**) and mid-thickness (**Fig. 10(e-h)**) regions of the samples. The major texture components observed in the different samples are indicated in **Fig. 10** and the color legend represents the maximum and minimum intensities by 'red' and 'blue' colors, respectively. A schematic diagram of a ϕ_2 = 45° ODF section showing ideal BCC orientations as expected in ferritic steel is presented as reference in **Fig. 10i**.

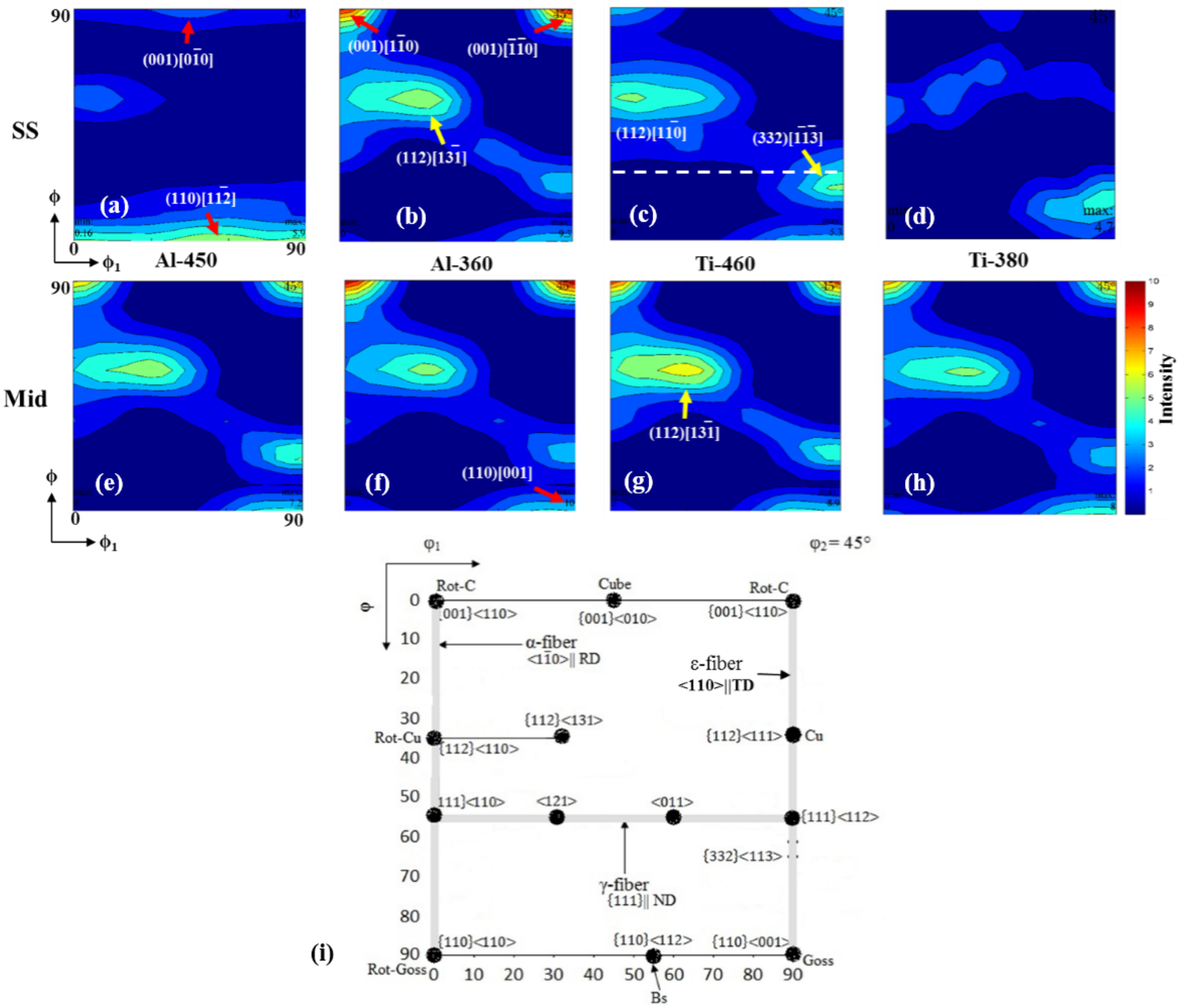

Fig. 10: Φ_2=45° ODF sections of the strip samples obtained from the macro-texture study at (a-d) sub-surface (SS) and (e-h) mid-thickness regions. The important texture components are indicated by red and yellow arrows, respectively. (i) Ideal Φ_2=45° section of the Euler space showing ideal BCC orientations (Bunge notation) along with different fibers observed in BCC materials.

The texture of all the samples was similar at the mid-thickness location as expected from plane-strain deformation of austenite and its transformation during cooling, **Fig. 10(e-h)**. The mid-thickness texture is comprised of different orientations like Rotated Cube ({001}<110>), from {112}<110> of RD-fiber (RD||<110>) to {112}<131>, Goss ({110}<001>), γ-fiber (ND//<111>), and ε-fiber components from {332}<113> to {441}<118>. The different strip samples showed different sub-surface textures, **Fig. 10(a-d)**. Al-450 contained some Cube ({001}<010>), Brass ({110}<112>) and Goss ({110}<001>), orientations at the sub-surface, **Fig. 10a**. Sub-surface textures of Al-360 and Ti-460 were similar to their corresponding mid-thickness textures, **Fig. 10(b, c)**. The sub-surface texture of Ti-380 was quite random with ε-fiber close to Goss being the only prominent orientation along with weak Cube orientation and {112}<110> component, **Fig. 10d**.

3.5 Evaluation of tensile properties

Engineering stress vs. engineering strain curves from the tensile tested specimens are presented in **Fig. 11a** and the tensile properties are summarized in **Table 3**. **Fig. 11a** and **Table 3** show that the strength (both YS and UTS) increased with the decrease in coiling temperature. Dependence of strength on coiling temperature was more sensitive in the Ti-treated samples (strength increased by 144 (YS) and 201 (UTS) MPa) in comparison to the Al-treated samples (strength increased by 86 (YS and UTS) MPa).

The increase in YS was accompanied by a continuous decrease in total elongation (TE) to failure. Ti-460 had the maximum TE followed by Al-450. It is interesting to note that the post-uniform elongation (Post-UE) was 2.5 – 4.2 times higher than the corresponding uniform elongation (UE) of the samples. Ti-460 showed the maximum TE, UE and even Post-UE, followed by Al-450. Ti-380 had the lowest ductility in all these respects. Tensile toughness was estimated from the area under the stress-strain curve. Ti-460 had the highest tensile toughness followed by Al-450, whilst Al-360 and Ti-380 had equally low tensile toughness, **Table 3**.

Logarithmic values of true-stress and true-strain are plotted in **Fig. 11b** to study the strain-hardening behavior. The samples showed two-stage strain-hardening and the strain-hardening exponent for each stage was calculated and is stated on **Fig. 11b**. Ti-380 had the highest n-values for both the hardening stages. The ‘n-value’ was also high for the second hardening stage of Ti-460. Strain-hardening ability and even formability of steel can be assessed by another parameter, i.e. YS:UTS ratio. Low YS:UTS ratio is preferred as it provides a larger stress range to perform the forming operation. Ti-380 had the lowest YS:UTS ratio of 0.74 whereas this ratio was within a close range (0.81-0.84) for the other samples.

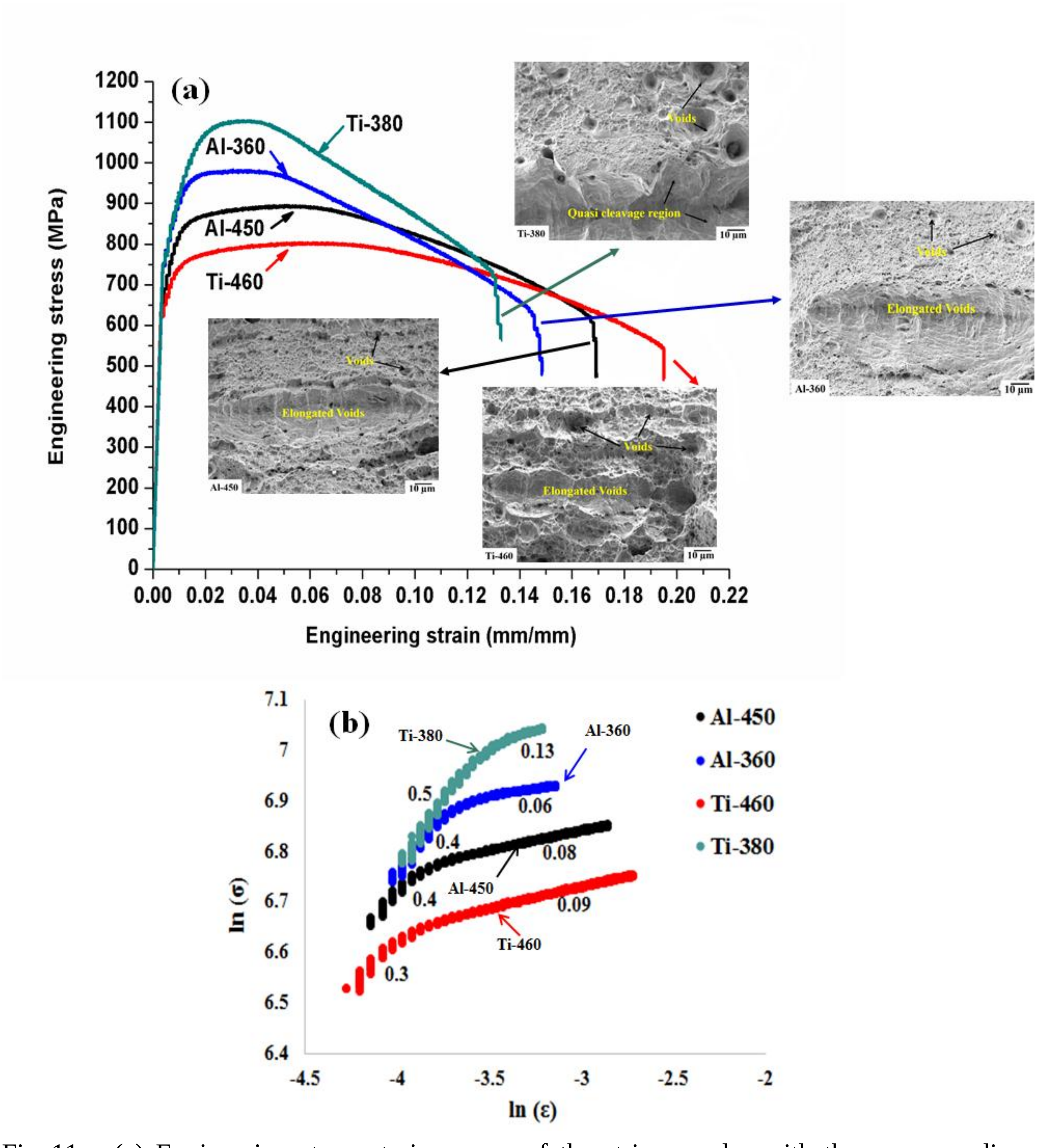

Fig. 11: (a) Engineering stress-strain curves of the strip samples with the corresponding fractographs given as inserts. (b) Logarithmic plots of the true-stress vs. true-strain for the determination of strain-hardening exponent (n).

The tensile fractographs of the samples are inserted in **Fig. 11a**. Presence of coarse and deep dimples, indicating greater extent of void growth, on the fracture surface of Ti-460 was in accordance with its high TE and post-UE. On the other hand, existence of cleavage and quasi-cleavage regions on the fracture surface of Ti-380 justified its low TE and Post-UE. Although coarse and elongated voids were present, the fracture surfaces of Al-450 and Al-360 were mostly covered by fine and shallow dimples. Such fine and shallow dimples, or dimple-sheets, were the outcome of extensive void nucleation but limited void growth, which contributed to limited ductility.

3.6 Evaluation of bending performance

Photographs of typical bend tested samples are illustrated in **Fig. 2a** and the average values of inner-bend-angle and minimum bend-radius to thickness ratio (R_{min}/t) are listed in **Fig. 2**. With minimum values of inner-bend-angle and R_{min}/t, Ti-460 showed the best bendability, followed by Al-360, Al-450 and Ti-380 in terms of inner bend angle. According to Hutchinson et al. [30] and Datsko et al. [31] the smaller the R_{min}/t ratio the better the bending performance of a material. Hutchinson et al. suggested R_{min}/t ratio to be maintained below 2.5 for ensuring satisfactory bending performance [30]. Although the best bending ratio obtained in the present study for Ti-460 sample is 3.7, this value may not be directly comparable with the earlier studies due to the difference in specimen size. The macroscopic views of the outer surfaces of the bend tested samples are given in **Fig. 2d**. Formation of cracks on the outer surfaces of the bend was studied at higher magnification as indicated in **Fig. 2d** by yellow arrows. Bend tested samples were further investigated by sectioning to view the cross section at the bend region, shown in **Fig. 2e**.

Only a few thin-cracks developed on the outer side of Ti-460, which showed the best bending performance. In contrast prominent and deep cracks appeared on the outer surfaces of both Al-450 and Ti-380, which had poor bendability. Al-360, which showed intermediate bending performance, contained multiple fine cracks along with a prominent crack, **Fig. 2d.** Visible cracks could not be detected on the inner surfaces of the bend tested specimens. The load vs. displacement plot for the bend tested samples in **Fig. 2f** showed that the samples failed at different points after reaching the peak load. Samples coiled at lower temperatures (Al-360 and Ti-380) followed a sudden and unstable drop from peak load indicating early failure. Al-450 sample also failed early during the bending test after a peak load lower than the other tested samples. Ti-460 sample, which showed the best bending performance, followed a gradual load drop even after the peak load associated with the stable growth of fine surface cracks which cause surface stretch marks without showing any macroscopic visual cracks.

In order to understand the damage mechanisms operating in the bend tested samples, cross-sections of the bend region were mounted, prepared metallographically and the regions beneath the outer surfaces were studied under SEM, **Fig. 12**. Al-450 showed a heavily strained microstructure with the presence of numerous voids, originated around carbides and MA constituents and also at the interfaces of different microstructural constituents, **Fig. 12a**. Localized deformation and shear band formation was noticed in Al-360 (dotted region in **Fig. 12b**) and the primary crack propagated along the shear band, **Fig. 12b**. In contrast, the microstructure at the outer bend layer of Ti-460 was more homogeneously deformed and the formation of very few defects was noticed around inclusions and occasionally along the interfaces of different constituents, **Fig. 12c**. The void formation was also limited in Ti-380. However transgranular cleavage micro-cracks were noticed inside the tempered martensite regions as shown by the insert in **Fig. 12d**. Although the steel was clean with low inclusion content, local void and crack formation from the hard and brittle Al_2O_3 inclusions and TiN particles was occasionally seen, but no link between inclusions and the main cracks were found in the investigated samples, **Fig. 12(e, f)**. The propagation of those defects depended on the matrix microstructure and its deformability and their location with regard to the macroscopic stress field.

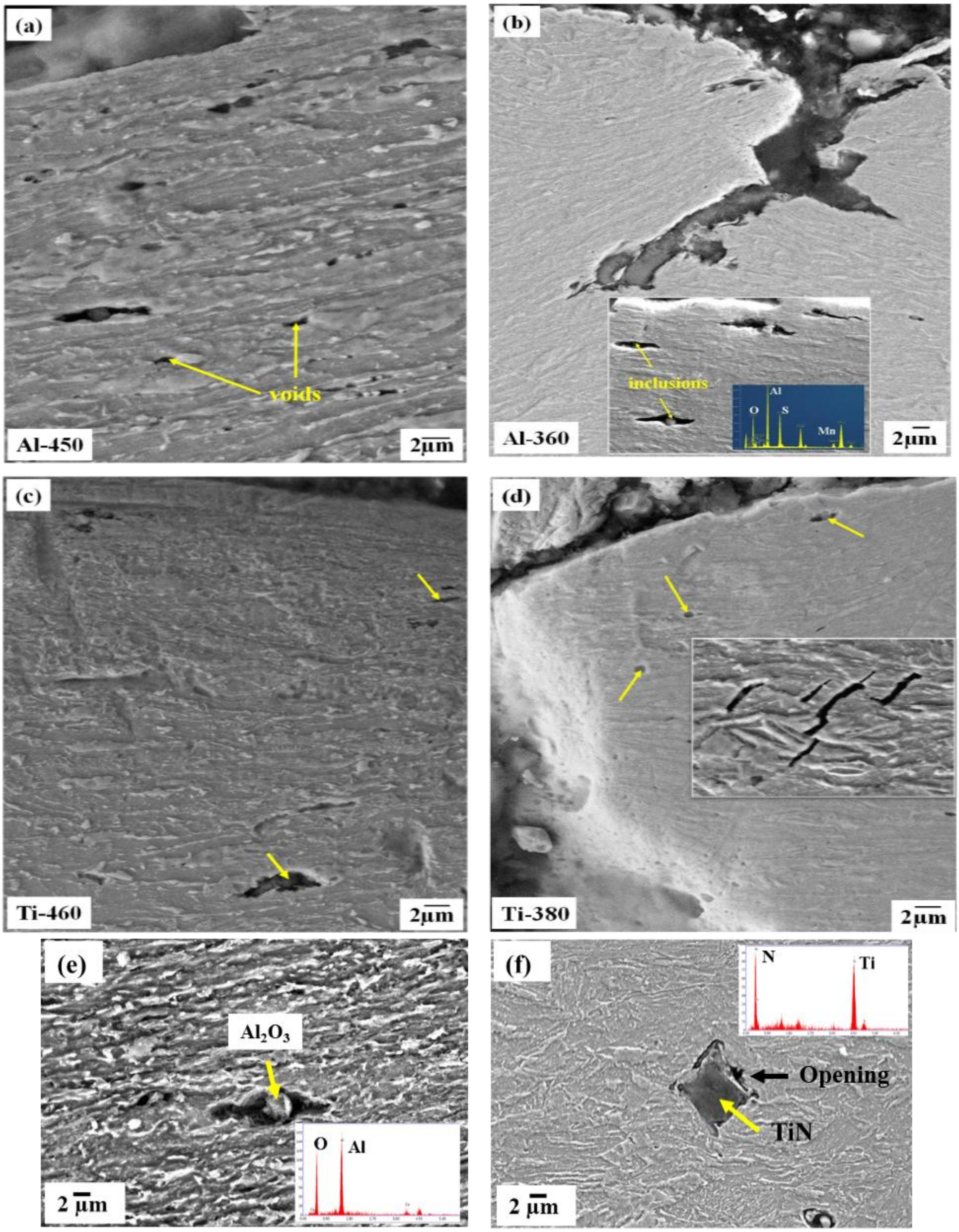

Fig. 12: SEM micrographs showing the generation of cracks along the transverse-section just beneath the fracture surface of (a) Al-450, (b) Al-360, (c) Ti-460 and (d) Ti-380 samples after bend testing. Yellow arrows indicated locations of voids or cracks in the microstructures of the bend tested samples. (e-f) Nucleation of cracks from the hard and brittle Al_2O_3 inclusions and TiN particles.

3.7 Assessment of bendability in view of processing, microstructure and texture

A comparative summary for the different samples considering microstructural features, hardness variation, texture, tensile and bending properties is given in **Table 4**. The microstructural constituents are divided into two major categories, softer (GB and UB) and harder (LB and TM). Total fraction of softer constituents was highest in Ti-460, followed by Al-450; this difference in microstructure between Ti-460 and Al-450 was due to the following reasons. First, there is a marginal difference in coiling start temperature 733 K (460 °C)] and 723 K (450 °C)], which may have influenced the amount of upper and granular bainite formed. Besides, the higher Ti level in the Ti-treated steel, along with Nb, consumed more C from the austenite solution to form complex (Ti,Nb)(C,N) as compared to in the Al-treated steel, with much lower Ti content. As a result, the C content in austenite was slightly lower in the Ti-treated steel (by 0.005 wt.% as predicted from Thermo-Calc®), over the range of 1073 K (800 °C) to the coiling temperatures, than that in the Al-treated steel reducing the hardenability and increasing the content of upper and granular bainite. Ti affects the microstructure in these steels in two ways. Firstly, it preferentially reacts with nitrogen to form TiN at high temperatures removing free nitrogen from the steel thereby retaining boron in solid solution (rather than allowing the formation of BN). Boron is known to have a strong effect on hardenability and therefore will affect the CCT diagram and microstructural constituents that form. Boron will therefore allow GB to form at high coiling temperatures in low carbon steels under natural cooling or continuous cooling. Secondly, presence of micro-alloying elements in solution can also promote the formation of GB [32]. Formation of carbide or carbo-nitride precipitation removes the interstitial elements from solution, which affects hardenability and can also contribute to the formation of softer constituents like GB and UB. This affect helps to explain the lower martensite fraction in the Ti treated steel at lower coiling temperature as compared to Al treated steel. These factors compete to influence the final microstructure, along with the role of prior austenite grain size / shape and coiling temperature. On the other hand the absence of AlN particles in the Al-treated steels raises a doubt about the effectiveness of B protection in that steel, although no BN was observed either (including during TEM studies). The GB fraction was lower in the Al-treated steel at higher coiling temperature, which may be due to the lack of B influence. The absence of nitride or carbo-nitride precipitation may retain more carbon / nitrogen in solution contributing to the formation of UB and TM. This may explain the higher martensite fraction in the Al-treated steel at lower coiling temperature as compared to Ti-treated steel.

The higher proportion of softer microstructure contributed to the best ductility and tensile toughness in Ti-460, at the expense of hardness and strength. Not only was the overall hardness low, the variation in hardness through the thickness was also small (within 20 VHN), **Fig. 8a**. Similarly, not only was the heterogeneity index (HI) at the sub-surface the least, its variation through the thickness was also small (within 1.5), **Fig. 8b**. The above factors encouraged uniform deformation not only at the microscopic scale, in a particular location, but also macroscopically over the entire strip thickness. A low overall hardness level with higher hardness at the sub-surface than the mid-thickness further ensured deformation uniformity as the surface layers preferentially deformed during bending.

Another important aspect that improved the bendability of Ti-460 is the similarity in texture between sub-surface and mid-thickness, **Fig. 10(c, g)**. The orientations found in this sample are listed in **Table 4**, along with the microstructures presented in **Figs. 4 and 5**, which indicate that the deformed austenite transformed during cooling and coiling operations through the thickness. The equation proposed by Boratto et al. [33] predicted the recrystallization stop temperatures (T_{NR}) of the Al-treated and Ti-treated steels to be ~ 1248 K (~ 975 °C) and ~ 1258 K (~ 985 °C), respectively. The slightly higher T_{NR} of the Ti-treated steel was due to the contribution of both higher Ti content in solution and higher volume fraction of Ti(C,N) particles, **Fig. 3**. Ti retards the recrystallization of austenite although, not as effectively as Nb [33,34]. Thus the finish rolling temperature is further below T_{NR} for the Ti-treated steel than the Al-treated steel. The texture components found in Ti-460 originated from the transformation of Brass ({110}<112>), Copper ({112}<111>), Goss ({110}<001>) and S ({123}<634>) textures in the deformed austenite. Among the transformed texture, γ-fiber (ND//<111>), {332}<113> and {112}<131> components are known to be beneficial for ductility, formability and toughness [35,36]. Those beneficial texture components are indicated by yellow arrows in **Fig. 10(a-h).** All these factors in combination not only facilitated the uniform plastic deformation but also promoted void growth, after defect generation. In addition, the moderate strain-hardening rate delayed void coalescence [37]. Finally at the outer 'tensile' surface the strain energy was released by the formation of multiple, thin, fibrous cracks instead of prominent deep cracking. The combination of all the above factors improved the tensile ductility and bendability of Ti-460.

Among the investigated samples, the lack of bendability of Al-450 and Ti-380 and intermediate bendability of Al-360 can be attributed to the following aspects.

- In spite of the fact that softer constituents dominated the sub-surface microstructure of Al-450, the distribution of microstructural constituents and their respective hardness were such that a high heterogeneity index developed there. Microstructural heterogeneity resulted in strain-partitioning and deformation incompatibility between the harder and softer constituents contributing to defect generation by interface separation, **Fig. 12a**. Numerous voids also formed around the MA constituents and carbide films due to the preferential deformation of GB and UB. Coalescence of those voids before sufficient growth led to premature failure during bending.
- Another aspect of concern in Al-450 was the dominance of Cube and Goss orientations in the transformed texture. Those textures are indicated by red arrows in **Fig. 10(a-h).** Such orientations are expected to originate from recrystallized austenite, instead of deformed austenite. The sub-surface microstructure of Al-450 also indicated the presence of recrystallized prior-austenite grains at the point of transformation along with few deformed prior-austenite grains, **Fig. 5**. The T_{NR} of Al-treated steel wasn't much higher than the FRT ~ 298 K (~ 25°C). Considering the variability in industrial processing parameters and the adiabatic heating of the heavily deformed surface layer, the possibility of austenite recrystallization at that location could not be ruled out. Cube and Goss orientations are known to be detrimental for ductility and toughness [35,38,39], and in turn bendability. Such orientations not only promote the unstable crack propagation along the {001} cleavage planes in BCC structures, but are also known to cause delamination and crack initiation by interface separation of adjacent crystals [33, 36. 37].
- Ti-380 not only had a high hardness level but also a significant hardness variation with high HI that reflected the microstructural heterogeneity. High fraction of martensite, presence of Cube texture along with coarse and brittle TiN particles as crack initiators (**Fig. 12f**) led to transgranular cleavage micro-cracking of martensite, affecting the bendability. The different / weaker surface texture would be consistent with a higher FRT (due to the fact this strip is thicker (8 mm) than the others (6 mm)) and therefore there is less deformation below T_{NR}.
- Harder microstructural constituents with low n-value and high HI at the sub-surface region of Al-360 imposed a detrimental effect on the bendability. On the

other hand, beneficial sub-surface texture promoted plastic flow and resulted in intermediate bendability.

Overall Ti treatment appeared to be more effective than Al treatment in retaining B in solution and utilizing its beneficial effect in ensure microstructural uniformity. Use of higher coiling temperature of 733 K (460 °C) was beneficial from bendability point of view for Ti treated steel due to the softer surface microstructure and superior uniformity in microstructure and texture at the local-scale as well as through the thickness, however a lower strength is seen. Finally the effect of post uniform elongation on bendability (**Fig. 13**) of the investigated materials showed that in general with the increase in post-uniform elongation the inner bend angle decreased, i.e. bendability increased. Although Al-450 had the second highest post-uniform elongation, its inhomogeneous distribution of microstructural constituents resulted in an inferior bendability. Thus it appears that the post-uniform elongation can be related to bendability.

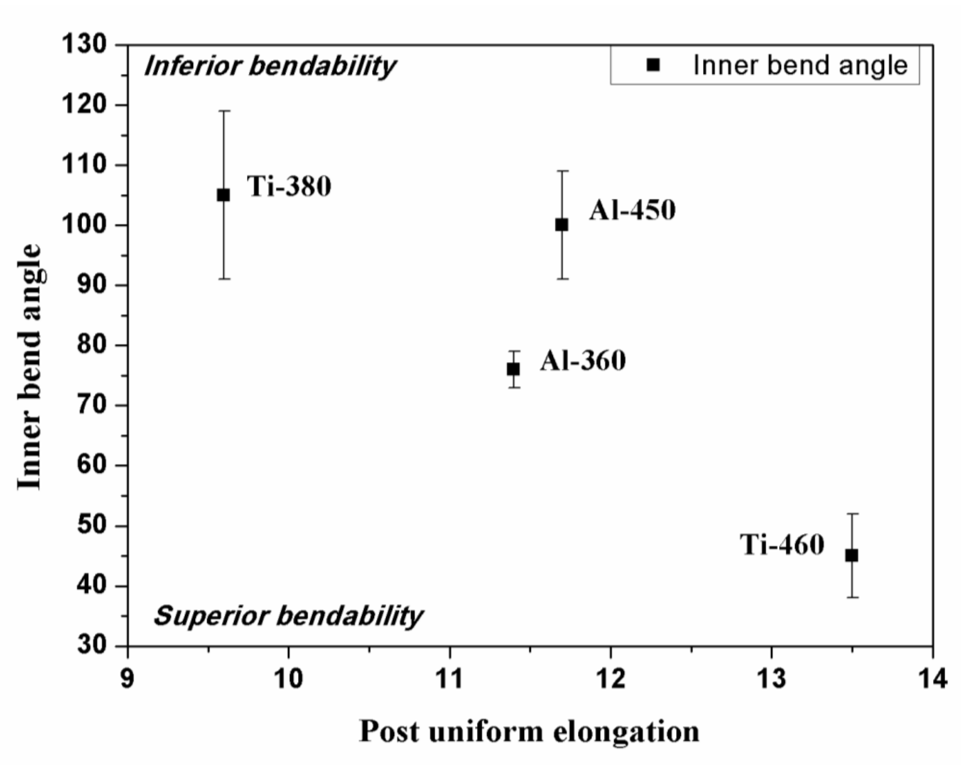

Fig. 13: Effect of post uniform elongation on the bendability of the investigated samples.

4. CONCLUSIONS

The conclusions of the present study can be considered in the context of other studies performed over the last two decades on the bending performance of high strength steels. The major findings of the present work are summarized below:

- Microstructure, hardness and their variations locally and through thickness along with the crystallographic texture at the sub-surface location plays the most important role on bendability. Defect generation during bending is associated with the separation of interphase boundaries or the strain-localization in form of shear-band and the associated shear cracking. Ensuring homogeneity in microstructure and minimum hardness variation at the local-scale in the sub-surface regions are therefore necessary for good bendability.
- Relatively softer and homogeneous microstructure containing granular bainite and upper bainite down to ~ 300-400 μm depth below the surfaces, generated at higher coiling temperature ~ 733 K (~ 460°C), is preferred for bendability. The upper bainite formed in the present study was relatively free from coarse MA films, which can be detrimental for bendability.
- Lower temperature coiling [633 K to 653 K (360 °C to 380 °C)] developed harder surface layers dominated by martensite along with the softer constituents. Such a microstructure is undesired as the steel acts like a dual-phase steel that is prone to shear cracking and interphase separation due to strain-localization.
- Lower hardness as well as less hardness variation at the sub surface region and throughout the thickness contributed to the best bending performance of the Ti treated sample coiled at 733 K (460 °C). Overall Ti treatment showed better microstructural uniformity as compared to Al treatment for B protection.
- Through thickness textural uniformity and presence of beneficial texture components such as γ-fiber, {332}<113> and even {112}<131> improve the bendability of rolled and coiled strip.
- Strain-hardening has a complex effect on bendability. High strain-hardening certainly delays defect generation. However, in particle containing systems where the particles facilitate defect generation, rapid hardening of the material can promote the propagation of the defect resulting in premature failure.

- In the presence of crack initiators like coarse and brittle TiN particles, hard microstructures and Cube and Goss texture in the sub-surface layer can cause local transgranular cleavage cracking.
- Finally the total elongation and post-uniform elongation obtained from tensile testing and bendability show a direct correlation.

Acknowledgements: Tata Steel in Europe, UK, for providing the Research Material and sharing industrial information of the subject, Department of Science and Technology, New Delhi, India, for the support of the research scholar Mr. Abhisek Mandal, research facilities developed at IIT Kharagpur through Institute SGDRI 2015 grant, finally Dr. Martin Strangwood from the University of Birmingham for providing valuable inputs at different stages of the work.

5. REFERENCES

1 M. Saiji, H. Kohei, and T. Yasush: *Newly-Developed Ultra-High Tensile Strength Steels with Excellent Formability and Weldability*, 2007.

2 K. Yamazaki, M. Oka, H. Yasuda, Y. Mizuyama, and H. Tsuchiya: *Recent Advances in Ultrahigh-Strength Sheet Steels for Automotive Structural Use*, Japan, 1995.

3 Y.B. Xu, Y.L. Bai, Q. Xue, and L.T. Shen: *Acta Materialia*, 1996, vol. 44, pp. 1917–26.

4 M. Kaupper and M. Merklein: *CIRP Annals - Manufacturing Technology*, 2013, vol. 62, pp. 247–50.

5 Z. Marciniak, J.. Duncan, and S.J. Hu: *Mechanics of Sheet Metal Forming*, 2nd editio., Elsevier Ltd, 2002.

6 E. Tempelman, H. Hercliff, and B.N. van Eyben: *Manufacturing and Design: Understanding the Principles of How Things Are Made*, 1st edn., 2014.

7 D. Rèche, T. Sturel, A.F. Gourgues-Lorenzon, and J. Besson: in *Strain Based Design of Pipelines*, 2010, pp. 1–8.

8 Liang Xue: *Engineering Fracture Mechanics*, 2010, vol. 77, pp. 1275–97.

9 J. Joutsenvaara: in *Proceedings of the METNET Seminar 2012 in Izmir*, T.R.

Department, ed., Kemi-Tornio University of Applied Sciences, 2012, pp. 19–29.

10 Y. Nagataki, S. Tsuyama, and Y. Hosoya: *Steel Research Laboratory*, 2013, vol. 99, pp. 245–53.

11 K. Hashiguchi: *Elastoplasticity Theory*, vol. 42, Springer Berlin Heidelberg, Berlin, Heidelberg, 2009.

12 W. Wang, M. Li, Y. Zhao, and X. Wei: *Materials and Design*, 2014, vol. 56, pp. 907–13.

13 M. Kuroda and V. Tvergaard: *European Journal of Mechanics - A/Solids*, 2004, vol. 23, pp. 811–21.

14 A.J. Kaijalainen, P. Suikkanen, L.P. Karjalainen, and J.J. Jonas: *Metallurgical and Materials Transactions A*, 2014, vol. 45, pp. 1273–83.

15 W. Wang, M. Li, Y. Zhao, and X. Wei: *Materials & Design (1980-2015)*, 2014, vol. 56, pp. 907–13.

16 M.D. M. Lie: *Philosophical Magazine A*, 2001, vol. 81, pp. 1997–2020.

17 J. R. Rice: in *Proceedings of the 14th International Congress on Theoretical and Applied Mechanics*, vol. 1, NorthHolland Publishing Co, 1976, pp. 207–20.

18 A. Maatta, A. Jarvenpaa, M. Jaskari, K. Mantyjarvi, and J.A. Karjalainen: *Material Forming - Esaform 2012, Pts 1 & 2*, 2012, vol. 504–506, pp. 901–6.

19 A.J. Kaijalainen, M. Liimatainen, V. Kesti, J. Heikkala, T. Liimatainen, and D.A. Porter: *Metallurgical and Materials Transactions A*, 2016, vol. 47, pp. 4175–88.

20 D. Rèche, T. Sturel, A.F. Gourgues-Lorenzon, and J. Besson: *Proceeding of European Conference of Fracture 18*, 2010, pp. 1–8.

21 A. Väisänen, K. Mäntyjärvi, and J.A. Karjalainen: *Key Engineering Materials*, 2009, vol. 410–411, pp. 611–20.

22 N. Pottore, N. Fonstein, I. Gupta, and D. Bhattacharya: *AHSSS Proc*, 2004, pp. 119–29.

23 G. Rosenberg, I. Sinaiová, P. Hvizdoš, and L. Juhar: *Metallurgical and Materials Transactions A*, 2015, vol. 46, pp. 4755–71.

24 K. Kawamura and K. Seto: *US Patent 20,130,048,151*, 2013, vol. 2, pp. 6–13.

25 A.-M. Arola, A. Kaijalainen, and V. Kesti: in *AIP Conference Proceedings*, vol. 1769, AIP Publishing LLC, 2016, p. 200024.

26 J. Sarkar, T.R.G. Kutty, D.S. Wilkinson, J.D. Embury, and D.J. Lloyd: *Materials Science and Engineering: A*, 2004, vol. 369, pp. 258–66.

27 T. Gladman: *The Physical Metallurgy of Microalloyed Steels*, Institute of Materials, 1997.

28 T. Siwecki, J. Eliasson, R. Lagneborg, and B. Hutchinson: *ISIJ International*, 2010, vol. 50, pp. 760–7.

29 H.K.D.H. Bhadeshia: *Bainite in Steels: Transformations, Microstructure and Properties*, IOM Communications, 2001.

30 B. Hutchinson, T. Siwecki, J. Komenda, J. Hagström, R. Lagneborg, J.-E. Hedin, and M. Gladh: *Ironmaking & Steelmaking*, 2014, vol. 41, pp. 1–6.

31 J. Datsko and C.T. Yang: *Journal of Engineering for Industry*, 1960, vol. 82, pp. 309–13.

32 S.-C. Wang and P.-W. Kao: *Journal of Materials Science*, 1993, vol. 28, pp. 5169–75.

33 F. Boratto, R. Barbosa, S. Yue, and J.J. Jonas: in *International conference on physical metallurgy of thermomechanical processing of steels and other metals*, Imao Tamura., ed., 1988, pp. 383–90.

34 M.G. Akben, T. Chandra, P. Plassiard, and J.J. Jonas: *Acta Metallurgica*, 1984, vol. 32, pp. 591–601.

35 R.K. Ray and J.J. Jonas: *International Materials Reviews*, 1990, vol. 35, pp. 1–36.

36 M.P. Butrón-Guillén, J.J. Jonas, and R.K. Ray: *Acta Metallurgica Et Materialia*, 1994, vol. 42, pp. 3615–27.

37 D.M. Tracey: *Engineering Fracture Mechanics*, 1971, vol. 3, pp. 301–15.

38 P. D. Wu, S. R. MacEwen, D. J. Lloyd, and K. W. Neale: *Effect of Cube Texture on Sheet Metal Formability*, vol. 364, 2004.

39 A.J. Kaijalainen, P.P. Suikkanen, L.P. Karjalainen, and D.A. Porter: *Materials Science*

and Engineering: A, 2016, vol. 654, pp. 151–60.

List of figures

Fig. 1: Schematic diagram of the thermomechanical processing schedule applied on the investigated strips along with the bainitic and martensitic transformation start temperatures as predicted from JMatPro® software. Bs - bainitic start temperature, Ms - martensitic start temperature, M_{50} - 50% martensite formation temperature M_f - martensite finish temperature. T_{NR}- Recrystallization stop temperature.

Fig. 2: (a-b) Schematic diagrams showing the orientation of the bend test specimens with respect to the strip and bend testing setup. (c) Macroscopic side-view of the bend tested specimens showing the minimum inner bend angles (until visible cracking and load-drop) with their values listed below along with the minimum bend ratio. (d) Corresponding macro-views of the cracks (at different magnifications) on the outer surface of the bend tested samples. (e) Showing the cracked regions mounted in Bakelite. (f) Load vs. displacement (at the middle of the specimen) plots obtained from bend testing.

Fig. 3: Prediction of precipitate volume fraction with temperature in (a) Al-treated and (b) Ti-treated steels as predicted from Thermo-Calc®.

Fig. 4: Optical micrographs of the region from the top-surface up to ~ 600 µm depth along the thickness direction of RD-ND plane of the Al-treated (Al-450 and Al-360) and Ti-treated (Ti- 460 and Ti-380) strips.

Fig. 5: Higher magnification scanning electron micrographs (SEM) of the investigated samples (mentioned within the respective image) at the sub surface region (~300-400µm from the top surface). Abbreviations: GB: Granular bainite, UB: Upper bainite, LB: Lower bainite, TM: Tempered martensite.

Fig. 6: Higher magnification SEM micrographs of (a) Ti-460 and (b) Al-360 samples. MA constituents are marked by yellow arrow. Abbreviations: GB: Granular bainite, UB: Upper bainite, LB: Lower bainite, TM: Tempered martensite.

Fig. 7: (a-f) Bright field, dark field, selected area diffraction patterns (SADP) and energy dispersive spectroscopy (EDS) of the investigated samples coiled at different temperatures as indicated by the sample codes given on the respective micrographs. The bainitic laths, martensitic laths and cementite precipitates are indicated by yellow, white and red arrows, respectively. SADP and EDS spectrums are taken from (Ti,Nb)(C,N), iron-carbide and vanadium carbide precipitates as given in figures (g-h). The precipitates are also marked in the corresponding images.

Fig. 8: (a) Average Vickers macrohardness through the thickness of the strip samples; (b) Variation in heterogeneity index (HI) through the thickness of the strip samples. Abbreviations: SS-1: Top sub surface, Qtr: Quarter thickness, Mid-Mid thickness and SS-2: Bottom sub surface.

Fig. 9: Hardness contour plots at the sub-surface region of the investigated strips (RD-ND plane). X-axis is in mm. and Y-axis is in µm. Color codes represent Vickers macrohardness values as given in the legends. Note that same hardness scale is used in all the plots.

Fig. 10: Φ_2=45° ODF sections of the strip samples obtained from the macro-texture study at (a-d) sub-surface (SS) and (e-h) mid-thickness regions. The important texture components are indicated by red and yellow arrows, respectively. (i) Ideal Φ_2=45° section of the Euler space showing ideal BCC orientations (Bunge notation) along with different fibers observed in BCC materials.

Fig. 11: (a) Engineering stress-strain curves of the strip samples with the corresponding fractographs given as inserts. (b) Logarithmic plots of the true-stress vs. true-strain for the determination of strain-hardening exponent (n).

Fig. 12: SEM micrographs showing the generation of cracks along the transverse-section just beneath the fracture surface of (a) Al-450, (b) Al-360, (c) Ti-460 and (d) Ti-380 samples after bend testing. Yellow arrows indicated locations of voids or cracks in the microstructures of the bend tested samples. (e-f) Nucleation of cracks from the hard and brittle Al_2O_3 inclusions and TiN particles.

Fig. 13: Effect of post uniform elongation on the bendability of the investigated samples.

Table 1: Chemical composition of the investigated steels (wt. %).

	C	**Mn**	**S+P**	**Si**	**Al**	**Ti**	**Cu+ Ni**	**Cr**	**Nb+Mo +V**	**B**	**N**
Al-treated	**0.117**	**1.571**	**0.014**	**0.057**	**0.068**	**0.003**	**0.030**	**0.503**	**0.322**	**0.0019**	**0.0046**
Ti-treated	**0.119**	**1.595**	**0.017**	**0.047**	**0.029**	**0.028**	**0.038**	**0.502**	**0.323**	**0.0019**	**0.0055**

Table 2: Fractions of microstructural constituents in the investigated samples as measured by image analysis.

Sample No.	Coiling Temperature [K (˚C)]	GB (vol. %)	UB (vol. %)	LB (vol. %)	TM (vol. %)
Al - 450	723 (450)	16 ± 4	59 ± 7	25 ± 2	-------
Al - 360	633 (360)	5 ± 2	13 ± 6	24 ± 2	58 ± 4
Ti - 460	733 (460)	25 ± 6	65 ± 5	10 ± 3	-------
Ti - 380	653 (380)	10 ± 2	12 ± 3	30± 3	48± 2

** GB-granular bainite; UB-upper bainite; LB-lower bainite; TM-tempered martensite.

Table 3: Tensile properties of the tested samples.

Sample ID	YS (in MPa)	UTS (in MPa)	TE (%)	UE (%)	Post-UE (%)	YS/UTS	Tensile toughness (MJ/ m^3)
Al - 450	722 ± 11	894 ± 8	16.7 ±1.2	4.5 ± 0.9	11.7 ± 0.72	0.81	139
Al - 360	808 ± 5	980 ± 12	14.5 ± 0.6	2.7 ± 1	11.4 ± 0.7	0.82	131
Ti - 460	670 ± 10	802 ± 12	19.5 ± 0.8	5.5 ± 0.1	13.5 ± 0.5	0.83	145
Ti - 380	814 ± 8	1103 ± 10	13.0 ± 0.2	2.8 ± 1.1	9.6 ± 0.9	0.74	131

Abbreviations: YS: Yield strength, UTS: Ultimate tensile strength, TE: Total elongation, UE: Uniform elongation, Post-UE: Post-uniform elongation, YS/UTS: yield strength to ultimate tensile strength ratio.

Table 4: Comparative assessment of microstructure, texture and mechanical properties of the investigated samples. * Softer constituents refers to upper and granular bainitic structures

Sample	**Microstructure ***	**Overall hardness through thickness**	**Heterogeneity Index (estimated from Hardness)**	**Sub-Surface Texture**	**Tensile properties**	**Bending property and R_{min}/t**	**Tensile fractography**	**Bend fractography**
Al-450	75% softer constituents.	Low. Harder sub-surface, softer mid-thickness.	Very high at sub-surface, low at mid-thickness	Cube, Brass, Goss and weak alpha fiber.	Low strength, intermediate ductility, n-value and tensile toughness.	Poor 8.82	Large and elongated dimples along with fine dimple sheet.	Prominent cracking.
Al-360	18% softer constituents.	High. Softer sub-surface, harder mid-thickness.	High at sub-surface, low at mid-thickness.	Rotated Cu to {112}<131>. Gamma fiber to {332}<113>. Some rotated Cube and Goss.	High strength, low ductility, n-value and tensile toughness.	Intermediate 6.23	Large and elongated dimples along with fine dimple sheet.	Prominent crack with several fine cracks.
Ti-460	90% softer constituents.	Lowest. Harder sub-surface, softer mid-thickness.	Low at sub-surface, comparatively higher at mid-thickness	Rotated Cu to {112}<131>. Gamma fiber to {332}<113>. Some rotated Cube and Goss.	Lowest strength, best ductility and tensile toughness. High-n during second stage.	Best 3.7	Relatively coarser and deeper voids.	Several fine cracks.
Ti-380	22% softer constituents.	High. Softer sub-surface, harder mid-thickness.	High at sub-surface, low at mid-thickness.	Weak texture of rotated Cu, transformed Cu and Cube.	Highest strength with lowest ductility and tensile toughness. High n-value.	Worst 10	Regions of quasi-cleavage fracture.	Prominent cracking.